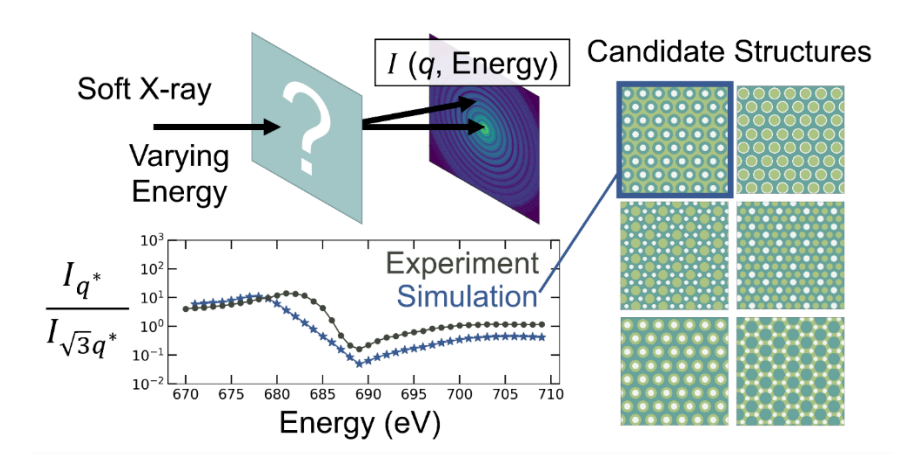
Simulation-guided analysis of resonant soft X-ray scattering for determining the microstructure of triblock copolymers

Veronica G. Reynolds, ^{a^} Devon H. Callan, ^{b^} Kumar Saurabh, ^e Elizabeth A. Murphy, ^{c,d} Kaitlin Albanese, ^c Yan-Qiao Chen, ^{ad} Claire Wu, ^b Eliot Gann, ^f Craig J. Hawker, ^{a,c,d} Baskar Ganapathysubramanian, ^e Christopher M. Bates, ^{a,b,c,d} Michael L. Chabinyc ^a

^aMaterials Department, ^bDepartment of Chemical Engineering, ^cDepartment of Chemistry & Biochemistry, ^dMaterials Research Laboratory, University of California, Santa Barbara, Santa Barbara, CA 93106, United States, ^eDepartment of Mechanical Engineering, Iowa State University, Ames, IA 50011, United States, ^fMaterials Measurement Laboratory, National Institute of Standards and Technology, Gaithersburg, MD 20899, United States [^]These authors contributed equally.

* To whom correspondence should be addressed: mchabinyc@engineering.ucsb.edu

Table of Contents Image:



TOC text. An efficient simulation code for Resonant Soft X-ray Scattering (RSoXS) was used to determine the structure of a model ABC triblock copolymer. Hard small angle X-ray scattering verified the structure pointing to the potential of fusing data sets across methods.

Abstract

Resonant soft X-ray scattering (RSoXS) probes structure with chemical sensitivity that is useful for determining the morphology of multiblock copolymers. However, the hyperspectral scattering data produced by this technique can be challenging to interpret. Here, we use computational scattering simulations to extract the microstructure of a model triblock copolymer from the energydependent scattering from RSoXS. An ABC triblock terpolymer formed from poly(4methylcaprolactone) (P4MCL), poly(2,2,2-trifluoroethylacrylate) (PTFEA), and poly(dodecylacrylate) (PDDA), P4MCL-block-PTFEA-block-PDDA, was synthesized as the model triblock system. Through quantitative evaluation of simulated scattering data from a physics-informed set of candidate structure models against experimental RSoXS data, we find the best agreement with hexagonally packed core-shell cylinders. This result is also consistent with electron-density reconstruction from hard X-ray scattering data evaluated against electron-density maps generated with the same model set. These results demonstrate the utility of simulation-guided scattering analysis to study complex microstructures that are challenging to image by microscopy.

Introduction

Block copolymers are a class of soft materials that self-assemble into mesocrystals, with applications ranging from nanoporous membranes to lithographic templates and drug-eluting coatings for biomedical devices.^{1,2} As the design space of multiblock copolymers grows through emerging synthetic methods that can address predictions from theory,^{3–6} there is a need for new characterization techniques that reveal greater structural insights than conventional methods provide.⁷ This is especially true as the number and type of blocks increases;⁸ for example, ABC triblock terpolymers form a significantly more diverse family of structures than AB diblocks.^{1,9} Moreover, beyond crystallographic ordering, these materials can exhibit fine subdomain structure on the nanoscale arising from the thermodynamics of self-assembly.⁷

Numerous methods are used to study and determine the nano/microstructure of block copolymers by leveraging a variety of mechanisms to achieve contrast between blocks. Transmission electron microscopy (TEM) produces images of very thin films with contrast determined primarily by relative electron densities. For organic materials, it is often necessary to enhance contrast by staining with a heavy metal, such as osmium or ruthenium, that selectively segregates into one domain; challenges then arise for multi-material systems in which certain components may be difficult to stain selectively (or at all). 10,11 Atomic force microscopy (AFM) maps the surface of a sample through height, phase, or viscoelasticity contrast, which may or may not reflect the bulk structure of a material. 12–14 Near-field scanning optical microscopy (NSOM)—a less common approach—can achieve sufficiently high resolution for imaging block copolymer self-assembly, but contrast often must be enhanced through fluorescence labeling or polarization modulation. 15,16

As a complement to real-space microscopy techniques, X-ray and neutron scattering probe structure in reciprocal space with contrast linked to chemical composition. X-ray scattering techniques record the intensity of a scattered beam as a function of angle, corresponding to different length scales represented in the structure of a material. Conventional, single-energy hard X-ray scattering reveals substantial structural information if the blocks have sufficient electrondensity contrast and long-range order. Neutron scattering frequently requires deuteration to enhance the scattering contrast between domains. Unlike these methods, resonant soft X-ray scattering (RSoXS, alternatively called anomalous scattering at hard X-ray energies) probes the structure of multiblock copolymers with chemical sensitivity by varying X-ray energy across elemental absorption edges. Resonant contrast is determined by differences in the dielectric function, linked to specific bonding environments present in a material.¹⁷ The resonance effect can improve the scattering signal from thin films, which typically exhibit a low intensity due to small sample volume.¹⁸ The energy dependence of RSoXS patterns is then linked to changes in the structure factor (e.g., two blocks each forming different lattices) and/or the form factor (e.g., a core-shell cylinder which alternately scatters as a solid or hollow cylinder depending on resonant contrast).^{19,20} In both cases, the scattering data must be compared to a model to determine an appropriate structure.

For systems with established structure models and contrast functions, RSoXS has been shown to access structural information unavailable to single-energy X-ray scattering. RSoXS performed at the carbon edge revealed structural details such as core—shell domains and nested hexagonal lattices of cylinders formed by a poly(1,4-isoprene)-*block*-polystyrene-*block*-poly(2-vinyl pyridine) triblock copolymer. ¹⁹ Another demonstration involving anomalous scattering at the bromine edge showed that in polystyrene-*block*-poly(4-hydroxystyrene) (PS-*b*-PHS), added

brominated PHS homopolymer segregated to the PS-PHS interface in a core-shell structure.²⁰ RSoXS is also valuable in studying membrane microstructures, where disentangling signals from microphase separation/chemical heterogeneity and void structure or surface roughness is challenging in single-energy measurements.^{21,22} One important feature in the resonant scattering of block copolymers is the variation in relative peak intensities with energy. Quantitative extraction of energy-variant parameters from RSoXS data has been used to determine the crystalline packing of conjugated polymers.²³ A similar quantitative approach to analyzing the resonant scattering of block copolymers would represent an advance in the interpretation of energy-dependent relative peak intensities. Computational scattering simulations of polarized resonant soft X-ray scattering (P-RSoXS) have been used to characterize molecular orientation at interfaces in organic photovoltaic donor–acceptor blends and polymer-grafted nanoparticles.^{24,25} By combining simulations and experiments, structure models can be quantitatively evaluated against experimental data.

Here, we present a technique for studying the structure of block copolymers using simulation-guided analysis of scattering data. Investigations into the structure of block copolymers are typically accompanied by microscopy to identify a single model that can be applied to interpret the data; instead, we leverage high-throughput computation to evaluate many models as an alternative. We used a new fast RSoXS pattern simulation software that exploits computational acceleration with graphics processing units (GPUs) to determine the structure of an ABC triblock terpolymer formed from poly(4-methylcaprolactone) (P4MCL), poly(2,2,2-trifluoroethylacrylate) (PTFEA), and poly(dodecylacrylate) (PDDA): P4MCL-block-PTFEA-block-PDDA (Figure 1). The RSoXS simulation software has been validated with various canonical and experimental results²⁵ for both isotropic and anisotropic materials and here we examine its use for a more

complex system. This triblock polymer has a useful chemical handle for RSoXS—the fluorine-containing PTFEA block exhibits high contrast relative to P4MCL and PDDA at the fluorine edge (685 eV). By evaluating the computational scattering data from a physics-informed set of candidate structure models against experimental scattering data, we determine the most likely structure to be hexagonally packed core—shell cylinders with a PDDA matrix, PTFEA shell, and P4MCL core. This conclusion is in good agreement with electron-density reconstruction of bulk small-angle X-ray scattering (SAXS) data evaluated against the electron-density maps derived from the same structure model set. In summary, we demonstrate an approach to scattering analysis which leverages computations to rapidly evaluate many models against experimental data.

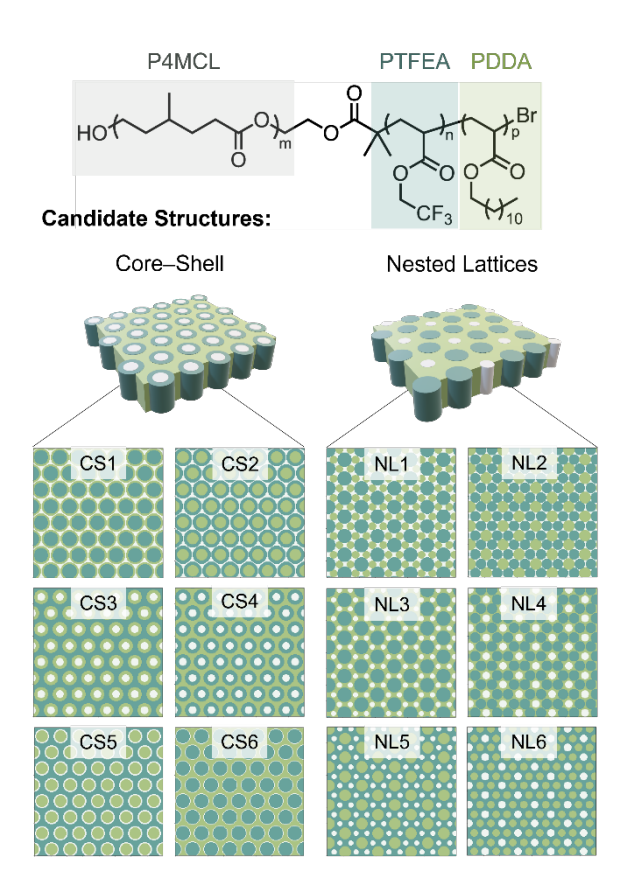


Figure 1. The set of candidate structure models includes two previously observed morphologies in ABC triblocks (core–shell cylinders and nested lattices). Within each type, there are 3! = 6

morphologies representing different arrangements of the blocks. All structure models were considered, irrespective of block ordering.

Experimental Methods

Synthesis & Characterization. The P4MCL-b-PTFEA-b-PDDA ABC triblock terpolymer was isolated by automated flash chromatography of a parent triblock, which produces well-defined fractions after separation with a low dispersity and negligible homopolymer impurities.³ The parent P4MCL-b-PTFEA-b-PDDA triblock was synthesized by sequential anionic ring-opening polymerization (ROP) and photo-initiated atom-transfer radical polymerization (photoATRP) starting from the bifunctional initiator 2-hydroxyethyl 2-bromoisobutyrate (HEBIB). Assynthesized triblock had molar masses of P4MCL, PTFEA, and PDDA = 14, 13, and 5.0 kg/mol, respectively, as calculated by end-group analysis using nuclear magnetic resonance (NMR) spectroscopy. The volume fractions of as-synthesized triblock, calculated from the block molar masses and homopolymer densities, are $\langle f_{P4MCL} \rangle = 0.48$, $\langle f_{PTFEA} \rangle = 0.33$, and $\langle f_{PDDA} \rangle = 0.19$. While the parent triblock morphology could not be definitively assigned by SAXS, the fractionated material with $f_{PAMCL} = 0.13$, $f_{PTFEA} = 0.51$, and $f_{PDDA} = 0.36$ exhibits clear reflections that index to a hexagonal crystal system. Based on the high-quality SAXS pattern, this fraction was identified as a candidate for RSoXS analysis. The PTFEA, P4MCL, and PDDA block chemistries were chosen because microphase separation is observed between all three pairs at reasonable degrees of polymerization, which is important for self-assembly kinetics. Each block has a low glass transition temperature ($T_{\rm g,P4MCL} \approx -60$ °C, $T_{\rm g,PTFEA} \approx 1$ °C; $T_{\rm g,PDDA}$ cannot be resolved due to an overlap with the melting temperature, but the homopolymer is a liquid under ambient conditions)^{26–28} and the resulting triblock is a soft solid which is readily annealed thermally or using solvent vapor.

Small-Angle X-ray Scattering. SAXS measurements of bulk samples were conducted using a custom-built SAXS diffractometer at the Materials Research Laboratory (MRL) X-ray facility (University of California, Santa Barbara). For these experiments, 1.54 Å Cu Kα X-rays were generated using a Genix* 50 W X-ray microsource (50 μm micro-focus) equipped with FOX2D collimating multilayer optics (Xenocs) and high-efficiency scatterless single-crystal/metal hybrid slits.

Thin Film Preparation. P4MCL-b-PTFEA-b-PDDA thin films for RSoXS were prepared by spin coating a 0.03 mass fraction solution of polymer in toluene directly onto a silicon nitride window (Norcada Inc.). To increase long-range order, the sample was solvent-vapor annealed for 1 hour using 1 mL of toluene in a 75 mL glass jar. The PLA-b-PTFEA diblock thin film sample produced for near-edge X-ray absorption fine structure (NEXAFS) spectroscopy measurement was prepared by spin coating a 0.05 mass fraction solution of polymer in chlorobenzene onto quartz and floating the film in deionized water onto a silicon nitride window. The diblock thin film had a thickness of 139 nm as measured by spectral reflectance (Filmetrics F20) on a separate section of the film floated onto silicon.

RSoXS and NEXAFS. RSoXS and NEXAFS measurements were collected at the Spectroscopy Soft and Tender (SST-1) beamline at the National Synchrotron Light Source II.²⁹ Measurements were taken in vacuum with the incident beam normal to the substrate. Two-dimensional scattering patterns were recorded on a charge-coupled device (CCD) detector sensitive to soft X-rays (greateyes GmbH). The sample was positioned such that the incident beam encountered the silicon nitride membrane before the polymer thin film.

Results and Discussion

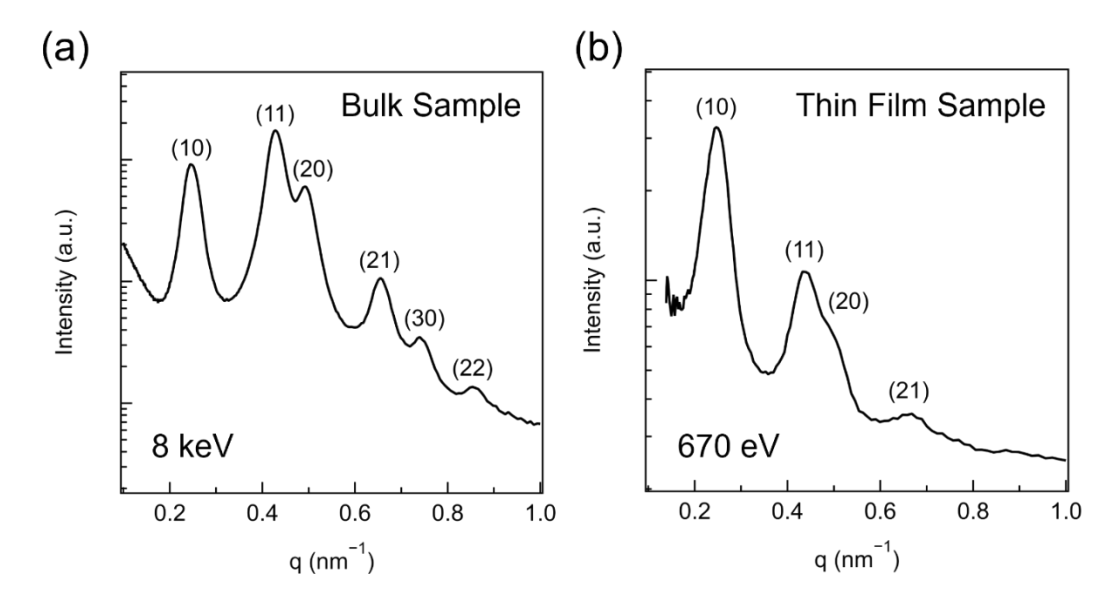


Figure 2. (a) Radially integrated hard (8 keV) X-ray scattering pattern of a P4MCL-*b*-PTFEA-*b*-PDDA bulk sample thermally annealed under vacuum at 130 °C for 12 h, 70 °C for 24 h, then room temperature for 5 h. (b) Radially integrated soft (670 eV) X-ray scattering pattern of a P4MCL-*b*-PTFEA-*b*-PDDA thin-film sample solvent vapor annealed using toluene for 1 h.

Examination of the scattering features from P4MCL-*b*-PTFEA-*b*-PDDA reveals the family of possible structures. In both bulk SAXS (**Figure 2a**) and thin-film RSoXS (**Figure 2b**), P4MCL-*b*-PTFEA-*b*-PDDA exhibits peaks at $q^*(10)$, $\sqrt{3}q^*(11)$, $\sqrt{4}q^*(20)$, $\sqrt{7}q^*(21)$. The relative peak intensities differ between these two measurements and are related to contrast between blocks at the hard (8 keV) and soft (670 eV) X-ray energies. The indexing of these peaks is indicative of a 2D hexagonal plane group $(p6mm)^{30}$ with a *d*-spacing $(2\pi/q^*)$ of 25 nm. This observation is consistent with two previously observed ABC triblock terpolymer morphologies: cylinders in a core–shell or nested lattice arrangement. ^{19,31,32} Using the *d*-spacing and NMR-derived volume fractions ($f_{P4MCL} = 0.13$, $f_{PTFEA} = 0.51$, $f_{PDDA} = 0.36$), a set of possible morphologies was generated through geometric analysis (**Figure 1**, see Supplementary Information for more details). Coreshell cylinders (CS) and nested lattices (NL) each have 3! = 6 possibilities (a permutation of blocks

A, B, and C as the matrix, core, and shell for core—shell cylinders or the matrix, lattice 1, and lattice 2 for nested lattices). These real-space models were used to create composition and electron-density maps to (a) generate the simulated scattering pattern for RSoXS analysis and (b) evaluate against the reconstructed electron-density maps, respectively. We stress that not all of these possible morphologies are physically realistic given the block connectivity of P4MCL-b-PTFEA-b-PDDA; as expected and demonstrated below, non-physical options are disfavored by our simulations.

Scattering Contrast. The key to interpreting scattering data from multi-material systems such as ABC triblock terpolymers is quantitatively understanding the origin of scattering contrast. The scattering contrast between blocks in conventional (hard X-ray) SAXS is determined by differences in electron density (0.342, 0.436, and 0.316 electrons per cubic angstrom for P4MCL, PTFEA, and PDDA respectively). Resonant contrast near atomic absorption edges is determined by differences in the energy-dependent complex index of refraction ($\hat{n}(E) = 1 - \delta(E) + i\beta(E)$). This results in the ability to probe structure with varying contrast between blocks; two particularly useful scenarios involve selectively probing a block by either minimizing contrast between the other two blocks (i.e., contrast matching) or maximizing contrast of the block relative to the other two (e.g., leveraging a unique heteroatom). P4MCL-b-PTFEA-b-PDDA is expected to have variations in contrast at both the carbon and fluorine K edges (284 eV and 685 eV, respectively). Here, we utilized the fluorine K edge because of the large and unambiguous contrast resulting from fluorine atoms in PTFEA and the enhanced resolution accessible at energies higher than the carbon K edge.

The refractive index of PTFEA was calculated from the absorption spectrum measured by transmission NEXAFS spectroscopy. This technique requires a thin film prepared on an X-ray transmissive substrate, e.g., silicon nitride. We found that PTFEA did not readily form a thin film, likely due to its surface energy, as spin coating resulted in severe dewetting (Supplementary Information, Figure S2). To perform the measurement, we instead used a diblock of PTFEA with poly(lactide) (PLA), PLA-b-PTFEA, which readily formed a suitable thin film (Supplementary Information, Figure S2). PLA-b-PTFEA was synthesized using sequential photoATRP and ROP from HEBIB (synthetic details available in the Supplementary Information). The imaginary part of the refractive index β of the diblock was calculated using Beer's law from the sample thickness, sample density, and optical density $(0.D. = -\ln(I/I_0))$ where I is the transmitted intensity through the sample and I_0 is the incident intensity, taken as the intensity measured through a blank silicon nitride substrate). 33 The real part of the refractive index δ was calculated via a Kramers-Kronig transform, using the open-source software KKcalc.³⁴ The refractive index of PTFEA was extracted by subtracting the PLA contribution (estimated using the Henke atomic scattering factors³⁵), assuming the index of refraction is a volume-fraction average ($\hat{n} = \sum_i \phi_i \hat{n}_i$, where \hat{n} is the complex index of refraction and ϕ is the volume fraction of each block i). Further details are provided in the Supplementary Information. The refractive indices of the two blocks without fluorine (P4MCL and PDDA) were estimated using Henke atomic scattering factors.³⁵ Figure S3 in the Supplementary Information shows the resulting optical constants for all three homopolymers. PTFEA has one broad absorption peak centered around 693 eV resulting from the trifluoromethyl groups. This feature provides a region of high contrast between both P4MCL-PTFEA and PDDA-PTFEA (see **Figure S4** for the pairwise contrast functions, $(\Delta \beta^2 + \Delta \delta^2)/\lambda^4$, where λ is the wavelength).

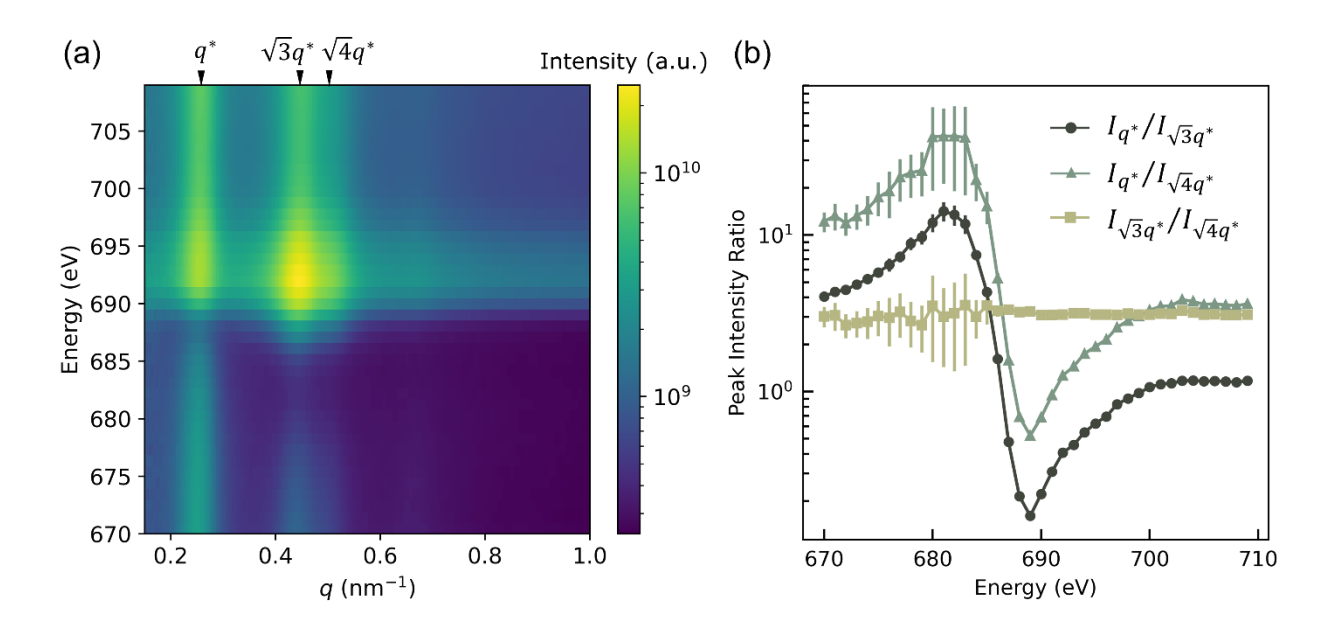


Figure 3. (a) Resonant soft X-ray scattering intensity of P4MCL-b-PTFEA-b-PDDA collected across the fluorine edge. (b) Pairwise peak intensity ratios show a strong energy dependence which is related to block contrast and structure. Error bars represent the standard error from peak fitting; larger error bars in the 670 eV to 685 eV range arise from challenges in fitting the low intensity $\sqrt{4}q^*$ peak.

Resonant Soft X-ray Scattering. The resonant soft X-ray scattering intensity of P4MCL-b-PTFEA-b-PDDA at energies spanning the fluorine absorption edge is shown in **Figure 3a**. As the X-ray energy is varied, there is a marked change in the relative intensities of different peaks (see **Figure S7** for the radially averaged scattering profiles and **Supplementary Movie S1** for an animation of the changing profile). The baseline, which is linked to X-ray fluorescence, 36 shifts significantly as well. The peak intensities at q^* , $\sqrt{3}q^*$, and $\sqrt{4}q^*$ were extracted at each energy by least-squares fitting Gaussian functions along with a cubic polynomial baseline (the intensity of the $\sqrt{7}q^*$ peak was too low to reliably fit). These three peaks were fit simultaneously to ensure a consistent baseline and to deconvolute the $\sqrt{3}q^*$ and $\sqrt{4}q^*$ peaks (further details are provided in the Supplementary Information and an example fit is shown in **Figure S8**). Peak intensity ratios were

calculated in a pairwise manner $(I_{q^*}/I_{\sqrt{3}q^*}, I_{q^*}/I_{\sqrt{4}q^*}, \text{ and } I_{\sqrt{3}q^*}/I_{\sqrt{4}q^*})$. Figure 3b shows the variation of these ratios across the fluorine absorption edge. We hypothesized that these energetic signatures could be used to identify the most likely structure among a set of models using computational scattering-pattern simulations.

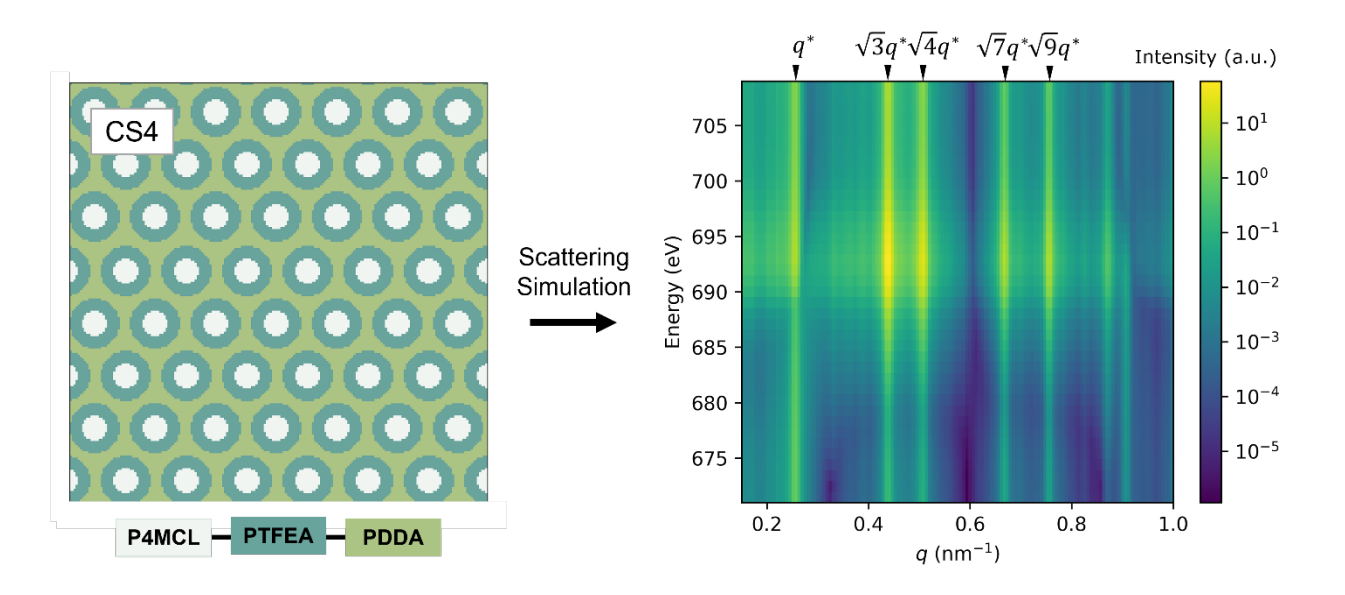


Figure 4. *Left*: Composition map representing a (200×200) voxel subset of the simulation input for model CS4. *Right*: Simulated resonant soft X-ray scattering intensity of structure model CS4 at energies across the fluorine edge.

Computational Scattering Pattern Simulations. Inputs to the scattering simulations are real-space composition maps of the models (**Figure 1**) and optical constants (δ and β of the complex index of refraction) of each block (**Figure S3**). The composition maps are composed of voxels (each representing 1 nm³) and are procedurally generated using custom code (hosted on GitHub, access available by request). This numerical approach enables greater flexibility for representing complex geometries relative to derived analytical models. Additionally, the voxel-based models do not need to be centrosymmetric—a common restriction for models considered in electron-density reconstruction in order to limit the number of possible reconstructions.³⁷ The scattering simulations

produce 2D scattering patterns with a resolution in reciprocal space determined by the dimensions of the input image. The simulations are fast due to the parallel processing of different energies; a 40-energy simulation with a $(1024 \times 1024 \times 1)$ voxel morphology takes ~ 8 s on the computing cluster used in this work. **Figure 4** shows an example of the simulated scattering intensity over energies across the fluorine edge for core–shell structure model CS4 (see Supplementary Information for the full set of scattering simulations, **Figure S9–S20**). The baselines of the simulated scattering profiles vary with energy in a similar manner to the experimental data, but one notable difference is the pronounced shape of the form factor visible in the simulated profiles. Because the simulated profiles have discrete peaks without overlap, peak intensities were extracted at specified q values rather than peak fitting. Then, the pairwise peak intensity ratios were calculated at each energy in a manner similar to the experimental data analysis.

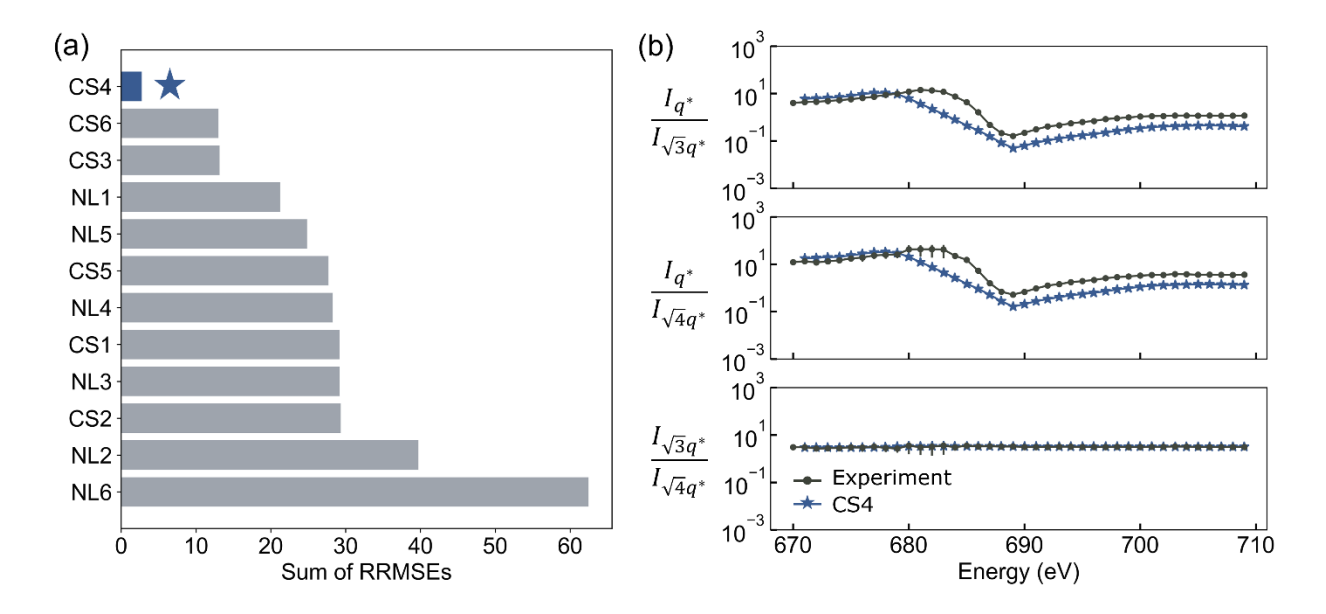


Figure 5. (a) Sum of the relative root-mean-squared errors of the natural logarithm of the intensity ratios for the simulation set evaluated against experimental data. (b) The energy-dependent intensity ratios, $I_{q^*}/I_{\sqrt{3}q^*}$ (top), $I_{q^*}/I_{\sqrt{4}q^*}$ (middle), and $I_{\sqrt{3}q^*}/I_{\sqrt{4}q^*}$ (bottom), of the best-matching simulation, CS4, plotted against experimental data. Error bars associated with the experimental data represent the standard error from peak fitting.

We determined the structure model that has the best fit by comparison of the measured-tosimulated peak intensity ratios. The simulated peak intensity ratios were evaluated against experimental data using a relative root-mean-squared error (RRMSE) of the natural logarithm of the ratios to accommodate the orders-of-magnitude variation in ratio values (see Supplementary Information for more details). The goodness-of-fit for each simulation was evaluated by summing the RRMSEs of the three ratios. **Figure 5** shows the goodness-of-fit ranking for the simulation set and the $I_{q^*}/I_{\sqrt{3}q^*}$, $I_{q^*}/I_{\sqrt{4}q^*}$, and $I_{\sqrt{3}q^*}/I_{\sqrt{4}q^*}$ ratios vs. energy for the best-fit structure model CS4 compared to experiment (a complete set of ratio overlays is available in the Supplementary Information, Figures S9–S20). The simulated scattering of CS4 fits well with respect to line shape and magnitude for all three ratios; in contrast, alternative structure models exhibited significantly different line shapes and/or magnitudes for some (CS6, Figure S14) or all (NL2, Figure S16) ratios. The best-matching model CS4 is a core-shell structure with a P4MCL core, PTFEA shell, and PDDA matrix. This block arrangement is consistent with the molecular connectivity of the P4MCL-b-PTFEA-b-PDDA triblock. The variation in peak intensity ratios for this core-shell structure represents differences in the form factor of the scattering bodies (circle-like vs. ring-like) as contrast changes with energy. Supplementary Movie S2 provides a visualization of this effect. For the $I_{q^*}/I_{\sqrt{3}q^*}$ and $I_{q^*}/I_{\sqrt{4}q^*}$ ratios, the simulation matches the inversion point observed experimentally around 689 eV and captures the line shape well, but it has a lower magnitude over much of the energy range. Two possible explanations for this are disorder and varying orientations of cylinders in the experimental sample, which can impact the relative peak intensities. The models represent cylinders oriented perpendicular to a substrate (X-ray beam parallel to the long axis of the cylinders) but the experimental sample is likely to contain crystalline domains at many orientations. The impact of this discrepancy is expected to manifest primarily in the magnitude of the peak intensity ratios (further discussion provided in the Supplementary Information). The $I_{\sqrt{3}q^*}/I_{\sqrt{4}q^*}$ ratio showed excellent agreement in line shape and magnitude between simulation and experiment.

Electron-Density Reconstruction from Hard X-ray Scattering. While hard X-ray scattering lacks the chemical sensitivity inherent to RSoXS, it is possible to extract information about the underlying electron-density distribution of the sample from SAXS data by evaluating potential distributions against a set of electron-density structure models. The relatively large number of peaks present in the bulk SAXS measurement (**Figure 2a**) and sufficiently high electron-density contrast enable reconstruction of the electron-density distribution by an inverse Fourier transform. ^{26,38,39} The electron density $\rho(x,y)$ of a two-dimensional morphology can be expressed by Fourier synthesis (Eqn. 1):

$$\rho(x,y) = \bar{\rho} + \sum_{hk}^{N} F_{hk} e^{2\pi i(hx+ky)} \tag{1}$$

where $\bar{\rho}$ is the average electron density in the unit cell, N is the number of reflections, x and y are the fractional coordinates in the unit cell, and F_{hk} is the structure factor at given Miller indices h and k (including all symmetry-equivalent reflections). The structure factor at a Bragg reflection hk is given by Eqn. 2:

$$F_{hk} = |F_{hk}|e^{i\varphi_{hk}} = A\sqrt{I_{hk}}e^{i\varphi_{hk}} \tag{2}$$

where I_{hk} is the integrated intensity with the appropriate Lorentz and multiplicity corrections, A is a scaling factor arising from the arbitrary intensity measured in scattering experiments, and φ_{hk} is the phase of the reflection. ^{40,41} Because scattering measurements only collect information about the amplitude of X-rays, phase is inherently ambiguous and solving the phase problem (i.e., determining φ_{hk} for each peak) is critical to determining the underlying unit cell. Since the

structure models considered here are all centrosymmetric, the values for φ_{hk} in Eqn. 2 are limited to 0 and π ($e^{i\varphi_{hk}} = \pm 1$, denoted as simply + or – in the following descriptions of phase combinations).⁴¹ The complexity of the phase problem is significantly reduced in this case as only the sign of each Fourier coefficient must be determined. The differences in reconstructed electron-density distributions originate from addition or subtraction (determined by phase) of each Fourier term. The expression for electron density can therefore be simplified to Eqn. 3:

$$\rho(x,y) = \bar{\rho} + A \cdot \sum_{hk}^{N} \pm \sqrt{I_{hk}} \cos(2\pi(hx + ky)) = \bar{\rho} + A\rho_{\varphi}(x,y)$$
(3)

where $\rho_{\varphi}(x,y)$ corresponds to the summation of Fourier terms over N reflections for a given set of phases. Although this expression for electron density is accurate in the limit as N approaches infinity, the finite number of reflections in the bulk SAXS data (N=6) necessitates an approximation of the reconstructed electron-density map by truncation of the Fourier series. Because of this truncation, all possible phase combinations can be enumerated for a total of $2^6=64$ and the corresponding electron-density maps can be readily calculated.

Reported procedures for the phase determination of similar morphologies via electron-density reconstruction often utilize prior chemical or physical information about the system to qualitatively determine the most likely phase combination. In many cases, a model is assumed or determined experimentally using supplementary characterization by microscopy. ^{39,40,42} Histogram-matching, a quantitative analysis which evaluates the distribution of discretized electron densities found in the reconstruction, ^{43–45} is insufficient as it does not consider the spatial distribution of electron density in the unit cell. Therefore, a simple yet quantitative approach to evaluating reconstruction results against many possible models is necessary. Here, we approach phase determination by quantitative evaluation of the structure model set against the phase combination set.

A set of model electron-density maps was generated from the 12 volume-fraction-informed structure models (**Figure 1**). These models assume perfect separation between blocks, which are represented as domains of constant electron density corresponding to the respective homopolymers. All 12 models were evaluated against 64 electron-density reconstructions for a total of 768 comparisons. Model—reconstruction pairs were evaluated by a least-squares regression analysis; each reconstruction was fit to each model by varying the scaling factor, A, to simultaneously minimize the squared error at each xy coordinate while conserving average electron density (Eqn. 4):

$$\min_{A} \sum_{xy} (\rho_{\text{model}} - \rho_{\text{reconstruction}})^2 = \min_{A} \sum_{xy} (\rho_{\text{model}} - \bar{\rho} - A\rho_{\varphi})^2$$
 (4)

By fitting to structure models, the block volume fractions and average electron density constraints inherent to the triblock are enforced. Poorly fitting reconstructions to the proposed structure models indicate an unphysical model or electron-density distribution. The coefficient of determination (R^2) was used as a goodness-of-fit metric for each model–reconstruction pair as shown in **Figure 6**. The matrix of R^2 values indicates how well each reconstructed electron-density distribution matches each structure model. The values of R^2 range from 0 to 1, with the best-fitting pairs (i.e., values of R^2 approaching 1) indicating electron-density distributions that closely match one of the volume-fraction-derived structure models. Code for electron-density reconstruction and model analysis is hosted on GitHub and available upon request.

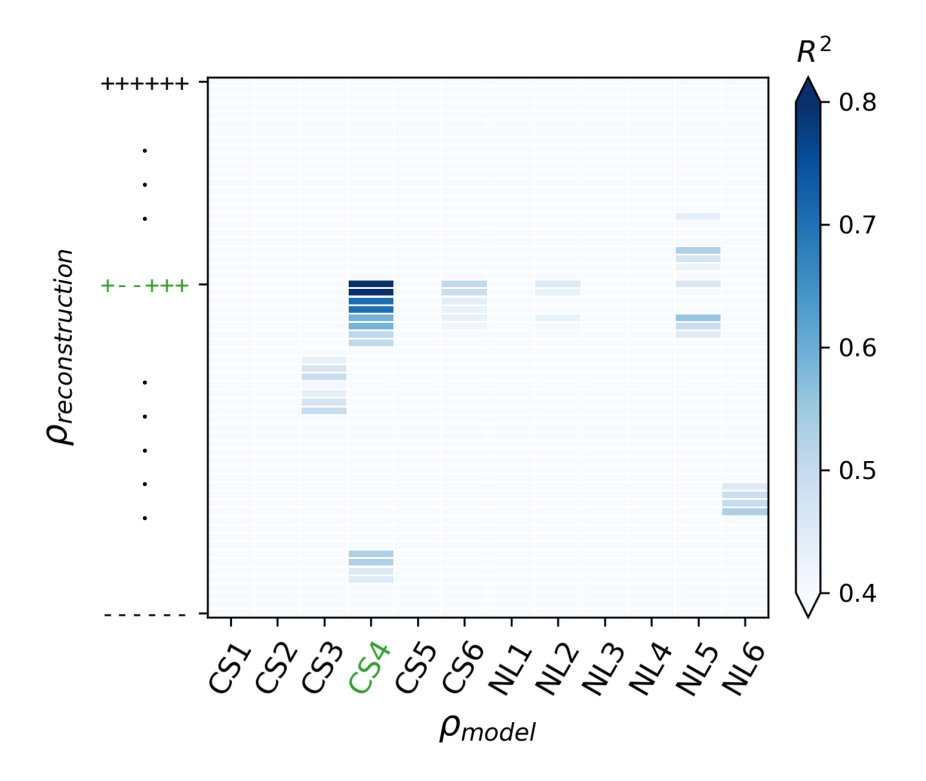


Figure 6. Coefficient of determination matrix (R^2) for each $\rho_{\text{model}} - \rho_{\text{reconstruction}}$ combination. The error between the electron density of the volume-fraction-derived model, ρ_{model} , and fitted electron-density reconstruction, $\rho_{\text{reconstruction}}$, is calculated at each xy coordinate. The best-fit model–reconstruction pair (CS4 and +--+++) is highlighted in green.

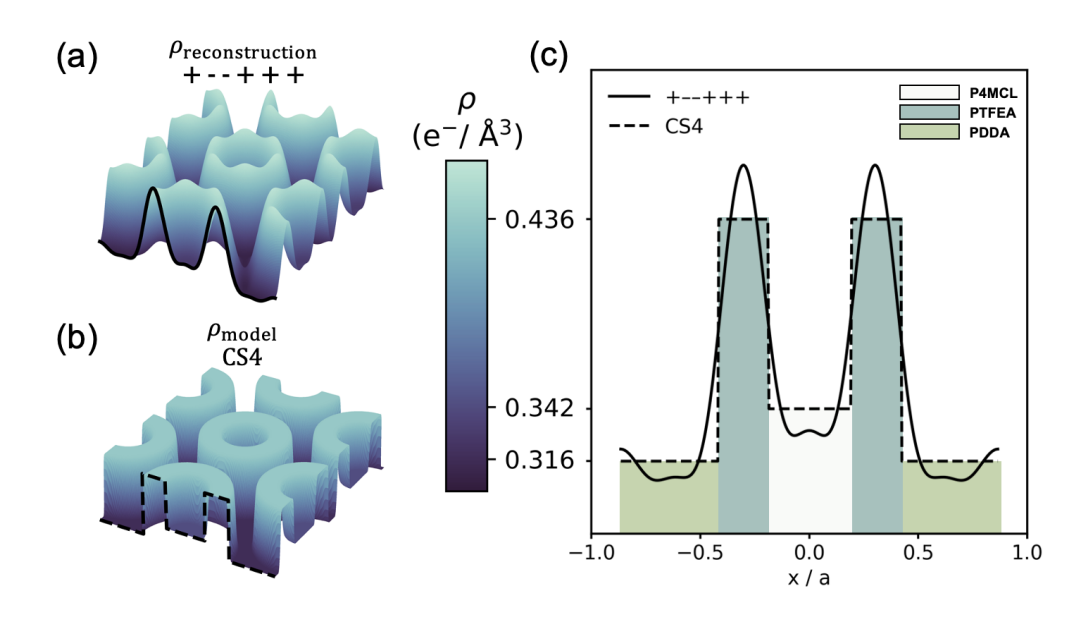


Figure 7. (a) Most likely electron-density reconstruction of bulk SAXS data using phase $\varphi = +--++++$. (b) Electron density of most likely core—shell structure model CS4 with a P4MCL core, PTFEA shell, and PDDA matrix. (c) 1D slice along the *x* axis (normalized by the lattice constant *a*) of the most likely reconstruction (solid) and model (dashed).

The best-fitting model—reconstruction pairs in **Figure 6** suggest CS4 (**Figure 7b**) as the most likely structure model, in agreement with the RSoXS analysis. This is further evidenced by the poor fits ($R^2 < 0.56$) of the other models to all possible reconstructions. We can also conclude that the reconstruction $\varphi = + - - + + +$ (**Figure 7a**) best matches the experimentally-determined block volume fractions and average electron density of the unit cell. Cross-sections of electron density from the CS4 model and reconstruction $\varphi = + - - + + +$ show good agreement (**Figure 7c**). The clustering of model—reconstruction pairs (**Figure 6**) for a given model is due to the minimal contributions of higher order peaks to the overall shape of the electron density distribution. Because hard X-ray scattering relies on electron-density contrast between domains, ⁴⁶ determining the three-phase ordering using this reconstruction technique is best suited to structures with maximal contrast between adjacent domains (e.g., if the P4MCL and PDDA blocks were adjacent, the low contrast between them may be limiting).

The simulation-guided RSoXS and hard X-ray electron-density reconstruction approaches can be used together to rank the model sets in a unified manner. Here we use two methods of comparison that are common for ranked lists. The rankings generated by each approach can be merged through the Schulze method, a comparison developed for determining a single winner from a set of votes of preference.⁴⁷ For the P4MCL-*b*-PTFEA-*b*-PDDA triblock, the two methods agree with CS4 as the structure of best fit. The merged ranking has CS6 as the second-most likely model and a tie between CS3 and NL5 in the spot following that. Although these approaches agreed on the best-fit structure model, the ranking order of models with higher-error disagreed strongly. The prevalence of discordant pairs between the two rankings is captured by a Kendall rank correlation coefficient that measures similarities of rankings. Here we obtain a coefficient of -0.24 which indicates a slight negative association of the rankings dominated by differences in the rank of

models with poor fits by each technique.^{48,49} The push toward data-driven integration of experiment, theory, and computation⁵⁰ and unique opportunities in dataset fusion^{51,52} suggest that exploration of methods to merge ranked lists from different experimental methods is a promising avenue to improve confidence in structural identification.

Conclusions

We developed an approach to hard and soft X-ray scattering analysis which leverages computational approaches to evaluate many structure models against experiments. The RSoXS analysis workflow combines scattering simulations and experiments to predict ABC triblock microstructure from the energy-dependent variation in peak intensity ratios. The results, based on pairwise ratios of the scattering peaks in RSoXS, show excellent agreement with electron-density reconstruction performed on bulk SAXS data. This agreement between RSoXS and SAXS on the best-fit model improves confidence in the assigned structure. Our approach to characterizing the microstructure of self-assembled thin films may be valuable in analyzing samples that are challenging to image by microscopy but have appropriate contrast in the soft X-ray regime, e.g., complex multiblock designs. The procedural generation of model structures and GPU-accelerated scattering simulations, paired with fast RSoXS measurement capabilities,²⁹ provide a means to rapidly extract microstructure for large block copolymer libraries. This demonstration of simulation-guided RSoXS analysis also acts as a benchmark for systems with more ambiguous scattering, such as semicrystalline polymers containing crystalline domains dispersed in an amorphous matrix.

Supplementary Information Description

Reagent information, synthetic methods, molecular characterization, automated flash chromatography method, optical microscopy of thin film samples for NEXAFS spectroscopy, refractive index calculation of mixtures, complex refractive indices and pairwise contrast functions of P4MCL, PTFEA, and PDDA, geometric derivations for structure models, radially-averaged RSoXS data, description of data reduction and peak fitting, complete set of scattering pattern simulations, relative root-mean-squared error calculation, discussion on the expected impact of varying cylinder orientation distributions.

Author Contributions.

V.G.R., D.H.C., K.S., E.A.M., K.A., Y.C., C.W., E.G., C.J.H., B.G., C.M.B., and M.L.C. designed experiments and wrote the paper. E.A.M., K.A., and Y.C. synthesized and characterized polymers. V.G.R., D.H.C., C.W., and E.G. prepared samples and performed the resonant soft X-ray scattering and near-edge X-ray absorption fine structure spectroscopy experiments. V.G.R., D.H.C., K.S., C.W., E.G., B.G., C.M.B., and M.L.C. developed and applied the computational methods.

Acknowledgement

This research was supported in part by the National Science Foundation through Award No. DMR-1808622 (RSoXS analysis) and under Award No. DMR-1844987 (Synthesis and SAXS). V.G.R. thanks the National Science Foundation Graduate Research Fellowship Program under Grant 1650114. BG and KS acknowledge support from Office of Naval Research under Award N00014-19-1-2453. This research used the Spectroscopy Soft and Tender (SST-1) beamline (7-ID-1) of the National Synchrotron Light Source II, a U.S. Department of Energy (DOE) Office of Science User Facility operated for the DOE Office of Science by Brookhaven National Laboratory under

Contract No. DE-SC0012704. Use was made of computational facilities purchased with funds from the National Science Foundation (CNS-1725797) and administered by the Center for Scientific Computing (CSC). The CSC is supported by the California NanoSystems Institute and the Materials Research Science and Engineering Center (MRSEC; NSF DMR 1720256) at UC Santa Barbara. The research reported here made use of shared facilities of the UC Santa Barbara MRSEC (NSF DMR-1720256), a member of the Materials Research Facilities Network (http://www.mrfn.org).

*Certain commercial equipment, instruments, software, suppliers or materials are identified in this paper to foster understanding. Such identification does not imply recommendation or endorsement by the National Institute of Standards and Technology, nor does it imply that the materials or equipment identified are necessarily the best available for the purpose.

References

- 1 C. M. Bates and F. S. Bates, *Macromolecules*, 2017, 50, 3–22.
- J. Bang, U. Jeong, D. Y. Ryu, T. P. Russell and C. J Hawker, *Adv. Mater.*, 2009, 21,
 4769–4792.
- 3 C. Zhang, M. W. Bates, Z. Geng, A. E. Levi, D. Vigil, S. M. Barbon, T. Loman, K. T. Delaney, G. H. Fredrickson, C. M. Bates, A. K. Whittaker and C. J. Hawker, *J. Am. Chem. Soc.*, 2020, **142**, 9843–9849.
- 4 M. R. Khadilkar, S. Paradiso, K. T. Delaney and G. H. Fredrickson, *Macromolecules*, 2017, **50**, 6702–6709.
- 5 Y. Zhu, M. R. Radlauer, D. K. Schneiderman, M. S. P. Shaffer, M. A. Hillmyer and C. K. Williams, *Macromolecules*, 2018, **51**, 2466–2475.
- 6 C. A. Tyler, J. Qin, F. S. Bates and D. C. Morse, *Macromolecules*, 2007, **40**, 4654–4668.
- A. Reddy, X. Feng, E. L. Thomas and G. M. Grason, *Macromolecules*, 2021, 54, 9223–9257.
- F. S. Bates, M. A. Hillmyer, T. P. Lodge, C. M. Bates, K. T. Delaney and G. H. Fredrickson, *Science*, 2012, **336**, 434–440.
- 9 N. Xie, M. Liu, H. Deng, W. Li, F. Qiu and A. C. Shi, *J. Am. Chem. Soc.*, 2014, **136**, 2974–2977.
- 10 C. Tang, J. Bang, G. E. Stein, G. H. Fredrickson, C. J. Hawker, E. J. Kramer, M. Sprung and J. Wang, *Macromolecules*, 2008, 41, 4328–4339.
- U. Breiner, U. Krappe, V. Abetz and R. Stadler, *Macromol. Chem. Phys.*, 1997, 198, 1051–1083.
- 12 V. Balsamo, S. Collins and I. W. Hamley, *Polymer*, 2002, **43**, 4207–4216.

- H. Elbs, K. Fukunaga, R. Stadler, G. Sauer, R. Magerle and G. Krausch, *Macromolecules*, 1999, **32**, 1204–1211.
- 14 S. Benaglia, C. A. Amo and R. Garcia, *Nanoscale*, 2019, **11**, 15289–15297.
- H. Aoki, Y. Kunai, S. Ito, H. Yamada and K. Matsushige, in *Applied Surface Science*, North-Holland, 2002, vol. 188, pp. 534–538.
- 16 M. J. Fasolka, L. S. Goldner, J. Hwang, A. M. Urbas, P. DeRege, T. Swager and E. L. Thomas, *Phys. Rev. Lett.*, 2003, **90**, 4.
- 17 B. A. Collins and E. Gann, *J. Polym. Sci.*, 2021.
- J. M. Virgili, Y. Tao, J. B. Kortright, N. P. Balsara and R. A. Segalman, *Macromolecules*, 2007, 40, 2092–2099.
- 19 C. Wang, D. H. Lee, A. Hexemer, M. I. Kim, W. Zhao, H. Hasegawa, H. Ade and T. P. Russell, *Nano Lett.*, 2011, **11**, 3906–3911.
- H. Hamamoto, H. Takagi, I. Akiba and K. Yamamoto, *Macromolecules*, 2021, **54**, 488–498.
- D. T. Wong, C. Wang, K. M. Beers, J. B. Kortright and N. P. Balsara, *Macromolecules*,
 2012, 45, 9188–9195.
- T. E. Culp, D. Ye, M. Paul, A. Roy, M. J. Behr, S. Jons, S. Rosenberg, C. Wang, E. W. Gomez, M. Kumar and E. D. Gomez, *ACS Macro Lett.*, 2018, 7, 927–932.
- G. Freychet, E. Gann, L. Thomsen, X. Jiao and C. R. McNeill, *J. Am. Chem. Soc.*, 2021,
 143, 1409–1415.
- E. Gann, B. A. Collins, M. Tang, J. R. Tumbleston, S. Mukherjee and H. Ade, *J. Synchrotron Radiat.*, 2016, **23**, 219–227.
- 25 S. Mukherjee, J. K. Streit, E. Gann, K. Saurabh, D. F. Sunday, A. Krishnamurthy, B.

- Ganapathysubramanian, L. J. Richter, R. A. Vaia and D. M. DeLongchamp, *Nat. Commun.* 2021 121, 2021, **12**, 1–10.
- C. Zhang, D. L. Vigil, D. Sun, M. W. Bates, T. Loman, E. A. Murphy, S. M. Barbon, J. A. Song, B. Yu, G. H. Fredrickson, A. K. Whittaker, C. J. Hawker and C. M. Bates, *J. Am. Chem. Soc.*, 2021, 143, 14106–14114.
- S. M. Barbon, J. A. Song, D. Chen, C. Zhang, J. Lequieu, K. T. Delaney, A. Anastasaki, M. Rolland, G. H. Fredrickson, M. W. Bates, C. J. Hawker and C. M. Bates, ACS Macro Lett., 2020, 9, 1745–1752.
- 28 J. L. Self, C. S. Sample, A. E. Levi, K. Li, R. Xie, J. R. De Alaniz and C. M. Bates, J. Am. Chem. Soc., 2020, 142, 7567–7573.
- E. Gann, T. Crofts, G. Holland, P. Beaucage, T. McAfee, R. J. Kline, B. A. Collins, C. R. McNeill, D. A. Fischer and D. M. DeLongchamp, *J. Phys. Condens. Matter*, 2020, **33**, 164001.
- 30 I. Hamley and V. Castelletto, in *Soft Matter Characterization*, Springer, Dordrecht, 2008, pp. 1021–1081.
- 31 H. Hückstädt, A. Göpfert and V. Abetz, *Polymer*, 2000, **41**, 9089–9094.
- H. Elbs, C. Drummer, V. Abetz and G. Krausch, *Macromolecules*, 2002, **35**, 5570–5577.
- 33 H. Yan, C. Wang, A. R. McCarn and H. Ade, *Phys. Rev. Lett.*, 2013, **110**, 177401.
- 34 B. Watts, Opt. Express, 2014, 22, 23628.
- 35 B. L. Henke, E. M. Gullikson and J. C. Davis, *At. Data Nucl. Data Tables*, 1993, **54**, 181–342.
- 36 T. Ferron, M. Pope and B. A. Collins, *Phys. Rev. Lett.*, 2017, **119**, 167801.
- I. W. Hamley, K. A. Koppi, J. H. Rosedale, F. S. Bates, K. Almdal and K. Mortensen,

- Macromolecules, 1993, 26, 5959-5970.
- 38 International Tables for Crystallography, Kluwer Academic Publishers, 1995.
- 39 M. Peterca, V. Percec, A. E. Dulcey, S. Nummelin, S. Korey, M. Ilies and P. A. Heiney, J. Am. Chem. Soc., 2006, 128, 6713–6720.
- 40 K. Flodström, C. V. Teixeira, H. Amenitsch, V. Alfredsson and M. Lindén, *Langmuir*, 2004, **20**, 4885–4891.
- 41 M. Impéror-Clerc, *Interface Focus*, 2012, 2, 589–601.
- 42 J. De, I. Bala, S. P. Gupta, U. K. Pandey and S. K. Pal, J. Am. Chem. Soc., 2019, 141, 18799–18805.
- 43 C. Baerlocher, L. B. McCusker and L. Palatums, *Zeitschrift fur Krist.*, 2007, **222**, 47–53.
- V. S. K. Balagurusamy, G. Ungar, V. Percec and G. Johansson, *J. Am. Chem. Soc.*, 1997,
 119, 1539–1555.
- V. Percec, M. Peterca, Y. Tsuda, B. M. Rosen, S. Uchida, M. R. Imam, G. Ungar and P.
 A. Heiney, *Chem. A Eur. J.*, 2009, 15, 8994–9004.
- 46 P. Garstecki and R. Hołyst, *Macromolecules*, 2003, **36**, 9191–9198.
- 47 M. Schulze, *CoRR*.
- 48 H. Abdi, *Encycl. Meas. Stat.*, 1955, 1–7.
- P. Virtanen, R. Gommers, T. E. Oliphant, M. Haberland, T. Reddy, D. Cournapeau, E.
 Burovski, P. Peterson, W. Weckesser, J. Bright, S. J. van der Walt, M. Brett, J. Wilson, K.
 J. Millman, N. Mayorov, A. R. J. Nelson, E. Jones, R. Kern, E. Larson, C. J. Carey, İ.
 Polat, Y. Feng, E. W. Moore, J. VanderPlas, D. Laxalde, J. Perktold, R. Cimrman, I.
 Henriksen, E. A. Quintero, C. R. Harris, A. M. Archibald, A. H. Ribeiro, F. Pedregosa, P.
 van Mulbregt, A. Vijaykumar, A. Pietro Bardelli, A. Rothberg, A. Hilboll, A. Kloeckner,

- A. Scopatz, A. Lee, A. Rokem, C. N. Woods, C. Fulton, C. Masson, C. Häggström, C. Fitzgerald, D. A. Nicholson, D. R. Hagen, D. V. Pasechnik, E. Olivetti, E. Martin, E. Wieser, F. Silva, F. Lenders, F. Wilhelm, G. Young, G. A. Price, G. L. Ingold, G. E. Allen, G. R. Lee, H. Audren, I. Probst, J. P. Dietrich, J. Silterra, J. T. Webber, J. Slavič, J. Nothman, J. Buchner, J. Kulick, J. L. Schönberger, J. V. de Miranda Cardoso, J. Reimer, J. Harrington, J. L. C. Rodríguez, J. Nunez-Iglesias, J. Kuczynski, K. Tritz, M. Thoma, M. Newville, M. Kümmerer, M. Bolingbroke, M. Tartre, M. Pak, N. J. Smith, N. Nowaczyk, N. Shebanov, O. Pavlyk, P. A. Brodtkorb, P. Lee, R. T. McGibbon, R. Feldbauer, S. Lewis, S. Tygier, S. Sievert, S. Vigna, S. Peterson, S. More, T. Pudlik, T. Oshima, T. J. Pingel, T. P. Robitaille, T. Spura, T. R. Jones, T. Cera, T. Leslie, T. Zito, T. Krauss, U. Upadhyay, Y. O. Halchenko and Y. Vázquez-Baeza, *Nat. Methods*, 2020, 17, 261–272.
- J. J. de Pablo, N. E. Jackson, M. A. Webb, L. Q. Chen, J. E. Moore, D. Morgan, R. Jacobs, T. Pollock, D. G. Schlom, E. S. Toberer, J. Analytis, I. Dabo, D. M. DeLongchamp, G. A. Fiete, G. M. Grason, G. Hautier, Y. Mo, K. Rajan, E. J. Reed, E. Rodriguez, V. Stevanovic, J. Suntivich, K. Thornton and J. C. Zhao, npj Comput. Mater., 2019, 5, 1–23.
- A. K. Singh, B. Ganapathysubramanian, S. Sarkar and A. Singh, *Trends Plant Sci.*, 2018, 23, 883–898.
- E. A. Huerta, G. Allen, I. Andreoni, J. M. Antelis, E. Bachelet, G. B. Berriman, F. B.
 Bianco, R. Biswas, M. Carrasco Kind, K. Chard, M. Cho, P. S. Cowperthwaite, Z. B.
 Etienne, M. Fishbach, F. Forster, D. George, T. Gibbs, M. Graham, W. Gropp, R.
 Gruendl, A. Gupta, R. Haas, S. Habib, E. Jennings, M. W. G. Johnson, E. Katsavounidis,
 D. S. Katz, A. Khan, V. Kindratenko, W. T. C. Kramer, X. Liu, A. Mahabal, Z. Marka, K.
 McHenry, J. M. Miller, C. Moreno, M. S. Neubauer, S. Oberlin, A. R. Olivas, D.

Petravick, A. Rebei, S. Rosofsky, M. Ruiz, A. Saxton, B. F. Schutz, A. Schwing, E. Seidel, S. L. Shapiro, H. Shen, Y. Shen, L. P. Singer, B. M. Sipocz, L. Sun, J. Towns, A. Tsokaros, W. Wei, J. Wells, T. J. Williams, J. Xiong and Z. Zhao, *Nat. Rev. Phys.*, 2019, 1, 600–608.